Injectable 2D Material-Based Sensor Array for Minimally Invasive Neural Implants

Kim, Jejung; Hong, Juyeong; Park, Kyungtai; Lee, Sangwon; Hoang, Anh Tuan; Pak, Sojeong; Zhao, Huilin; Ji, Seunghyeon; Yang, Sungchil; Chung, Chun Kee; Yang, Sunggu; Ahn, Jong-Hyun

Published in:
Advanced Materials

Published: 08/08/2024

Document Version:
Final Published version, also known as Publisher's PDF, Publisher's Final version or Version of Record

Published version (DOI):
10.1002/adma.202400261

Publication details:
Kim, J., Hong, J., Park, K., Lee, S., Hoang, A. T., Pak, S., Zhao, H., Ji, S., Yang, S., Chung, C. K., Yang, S., & Ahn, J.-H. (2024). Injectable 2D Material-Based Sensor Array for Minimally Invasive Neural Implants. *Advanced Materials*, *36*(32), Article 2400261. https://doi.org/10.1002/adma.202400261

ADVANCED MATERIALS
www.advmat.de

Injectable 2D Material-Based Sensor Array for Minimally Invasive Neural Implants

*Jejung Kim, Juyeong Hong, Kyungtai Park, Sangwon Lee, Anh Tuan Hoang, Sojeong Pak, Huilin Zhao, Seunghyeon Ji, Sungchil Yang, Chun Kee Chung, Sunggu Yang, and Jong-Hyun Ahn**

Intracranial implants for diagnosis and treatment of brain diseases have been developed over the past few decades. However, the platform of conventional implantable devices still relies on invasive probes and bulky sensors in conjunction with large-area craniotomy and provides only limited biometric information. Here, an implantable multi-modal sensor array that can be injected through a small hole in the skull and inherently spread out for conformal contact with the cortical surface is reported. The injectable sensor array, composed of graphene multi-channel electrodes for neural recording and electrical stimulation and MoS_2-based sensors for monitoring intracranial temperature and pressure, is designed based on a mesh structure whose elastic restoring force enables the contracted device to spread out. It is demonstrated that the sensor array injected into a rabbit's head can detect epileptic discharges on the surface of the cortex and mitigate it by electrical stimulation while monitoring both intracranial temperature and pressure. This method provides good potential for implanting a variety of functional devices via minimally invasive surgery.

1. Introduction

In recent years, there has been a continual increase in various brain diseases such as epilepsy, Parkinson's disease, Alzheimer's disease, and stroke. Consequently, technologies to effectively diagnose and treat severe brain diseases have emerged to become a crucial part of our healthcare system.[1–3] One such advancement is the neural recording system capable of monitoring electrocorticography (ECoG) signals over large areas of the cortical surface. These ECoG systems have been proven to be critical diagnostic and therapeutic instruments for patients suffering from severe epileptic seizures.[4,5] However, to pinpoint the seizure foci, surgical procedures, such as craniotomy and durotomy, are often required over a large cortical area to slide wide-dimensioned ECoG electrodes into the exposed cortex.[6–11] While these procedures are essential, they often result in considerable post-surgical symptoms, including cerebral edema, brain swelling, cerebral hemorrhage, and their resultant changes in intracranial pressure (ICP) and temperature (ICT).[12–15] Therefore, monitoring technologies for ICP and ICT are frequently employed to diagnose such symptoms. However, these sensors typically feature bulky designs that require intracranial access, potentially limiting patient mobility and impairing brain functions.

J. Kim, J. Hong, K. Park, A. T. Hoang, S. Ji, J.-H. Ahn
School of Electrical and Electronic Engineering
Yonsei University
Seoul 03722, Republic of Korea
E-mail: ahnj@yonsei.ac.kr
S. Lee, S. Yang
gBrain Inc.
Incheon 21984, Republic of Korea

S. Pak, H. Zhao, S. Yang
Department of Neuroscience
City University of Hong Kong
83 Tat Chee Avenue, Kowloon Hong Kong
C. K. Chung
Department of Neurosurgery
Seoul National University Hospital
Seoul 03080, Republic of Korea
C. K. Chung
Neuroscience Research Institute
Seoul National University College of Medicine
Seoul 03080, Republic of Korea
S. Yang
Department of Nanobioengineering
Incheon National University
Incheon 22012, Republic of Korea

The ORCID identification number(s) for the author(s) of this article can be found under https://doi.org/10.1002/adma.202400261

DOI: 10.1002/adma.202400261

Moreover, the need for separate devices to monitor different biosignals further complicates both the surgical and post-surgical processes.

In this article, we propose a minimally invasive, multimodal sensor array on a flexible mesh substrate that can be safely injected through a small hole in the skull to reduce the substantial surgical risks of craniotomy while achieving accurate neural monitoring. A small skull hole of 1–2 mm in diameter is sufficient for the device to be injected into the subdural space between the dura mater and the arachnoid mater where it subsequently unfolds itself to conformally attach to the cortical surface. The sensor array thereby achieves reduced surgical risk and provides conformal coverage of the cortical surface through a planar deployment configuration, compared to previous methods.[15–18] It also aims to streamline the entire process of diagnosis, treatment, and post-operative monitoring of brain diseases via the recording of multichannel ECoG signals, administering electrical stimulation, and monitoring ICP and ICT. The core sensing materials in the device, graphene, and MoS_2, are suitable for this application. Their atomically thin and highly flexible characteristics ensure that the sensors based on these materials will withstand the significant deformation exerted when the device is injected through the small tip of the syringe.[19–21] Moreover, the outstanding electrochemical performance and biocompatibility of graphene and the piezoresistive, temperature-dependant properties of MoS_2 enables stable, low-noise monitoring in the long term.[19–23] The sensor array will not only enable minimal invasiveness and low surgical risk but also allow for stable, long-term multimodal sensing and treatment of patients.[24,25]

2. Results and Discussion

2.1. Design of the Injectable Multimodal Sensor

The sensor array is injected by an air dispenser to be precisely administrated into the subdural space through a small hole in the skull. Once injected, it promptly spreads out and conformally adheres to the cortical surface (**Figure 1**a,b). The device is comprised of three main components: 1) a multimodal sensor array for ECoG, ICP, ICT monitoring, and electrical stimulation; 2) a long interconnect; 3) electrical pads for external connectivity with an injection stopper structure (Figure 1c). For optimal performance, the device should retain both its structural integrity and electrical properties even when it crumples to fit the narrow syringe tip of 1–2 mm. In addition, it should swiftly unfold to regain its original shape within the confined space of ≈10 mm from the syringe's tip to the cortical surface (Figure S1, Supporting Information text 2).[26–28] To achieve this, the device design incorporates a polymer-based radial mesh structure augmented by a strategically placed ribs structure and wide stimulation pads. The rib structure, along with the substrate of the device, exerts a uniformly distributed elastic restoring force for both structural stability and sufficient post-injection unfolding. The flexible mesh structure and wide stimulation pads alleviate the strain applied during the injection process. For post-injection interfacing with external readout devices, the long interconnects are terminated with electrical pads and an integrated injection stopper structure to stop the pads from being injected into the cranium.

The multimodal sensor array is composed of graphene-based electrodes for ECoG monitoring and electrical stimulation and MoS_2-based sensors for ICP and ICT monitoring (Figure 1d; Figures S2 and S3, Supporting Information). The chemical vapor deposition (CVD)-grown graphene used in the electrodes facilitates stable, precise measurements of ECoG signals and electrical stimulation with a high signal-to-noise ratio (SNR) for over 10 days (Figures S4a,b and S5, Supporting Information).[19,24,25,29] This is primarily attributed to the outstanding low contact impedance interface between the graphene-based electrodes and the cortical surface and the electrochemical stability of graphene in biological environments.[24] Its intrinsic mechanical flexibility also ensures that the electrodes remain unharmed. To further minimize the impedance of the electrode, 4-layer graphene was used for the contact region with the cortical surface with interconnects composed of Au (top image of Figure 1e,f).[22] For the ICT and ICP sensors, atomically thin metal organic chemical vapor deposition (MOCVD)-grown MoS_2 was used as a semiconducting sensing channel (middle and bottom images of Figure 1e). For temperature sensing, the MoS_2 sensing channel was formed on interdigitated gold electrodes and exhibited enhanced sensitivity and precise detection of temperature within the standard intracranial temperature range. The piezoresistive MoS_2 pressure sensor with serpentine structure effectively measured the strain induced by intracranial pressure. Both pressure and temperature sensors also exhibited high stability for up to 10 days, with an average impedance change of 0.19 ± 0.12% and 0.09 ± 0.06%, respectively (Figure S4c,d, Supporting Information). By leveraging the combination of ribs-reinforced mesh structures and two-dimensional (2D) materials known for their outstanding mechanical properties, the device achieves sufficient flexibility and elasticity to function as a multimodal injectable sensor array (Figure 1g).

2.2. Stability of Sensor Array During Syringe Injection

For a comprehensive analysis of the mechanics, we conducted an injection experiment of the mesh-structured device substrates using a human brain model made of agarose gel, known to exhibit similar mechanical and surface properties with the brain surface (**Figure 2**a; Figure S1, Video S1, Supporting Information).[30,31] Using an air dispenser and syringe, the sensor array was injected into an artificial brain through a small hole of 1–2 mm diameter in the skull. Here, the mesh-structured sensor array typically bends perpendicular to the injection direction. As the device substrate is propelled toward the tiny ≈1 mm diameter tip of the syringe by the medium solution and air pressure, it undergoes severe bending deformation, leading to high strain on device substrates. Such severe deformation may degrade the electrical performance or destroy electrodes, sensors, and substrates. This necessitates a thorough evaluation of the mechanics of the device to ensure stable operation of the device.

Two key parameters, injection pressure and unfolding area fraction, were evaluated during the injection (Figure S6, Supporting Information text 1). Adequate injection pressure—primarily decided by the bending stiffness of the device—is required for the contracted device substrate to be effectively ejected from the syringe, unfold, and adhere to the cortical surface. However, it

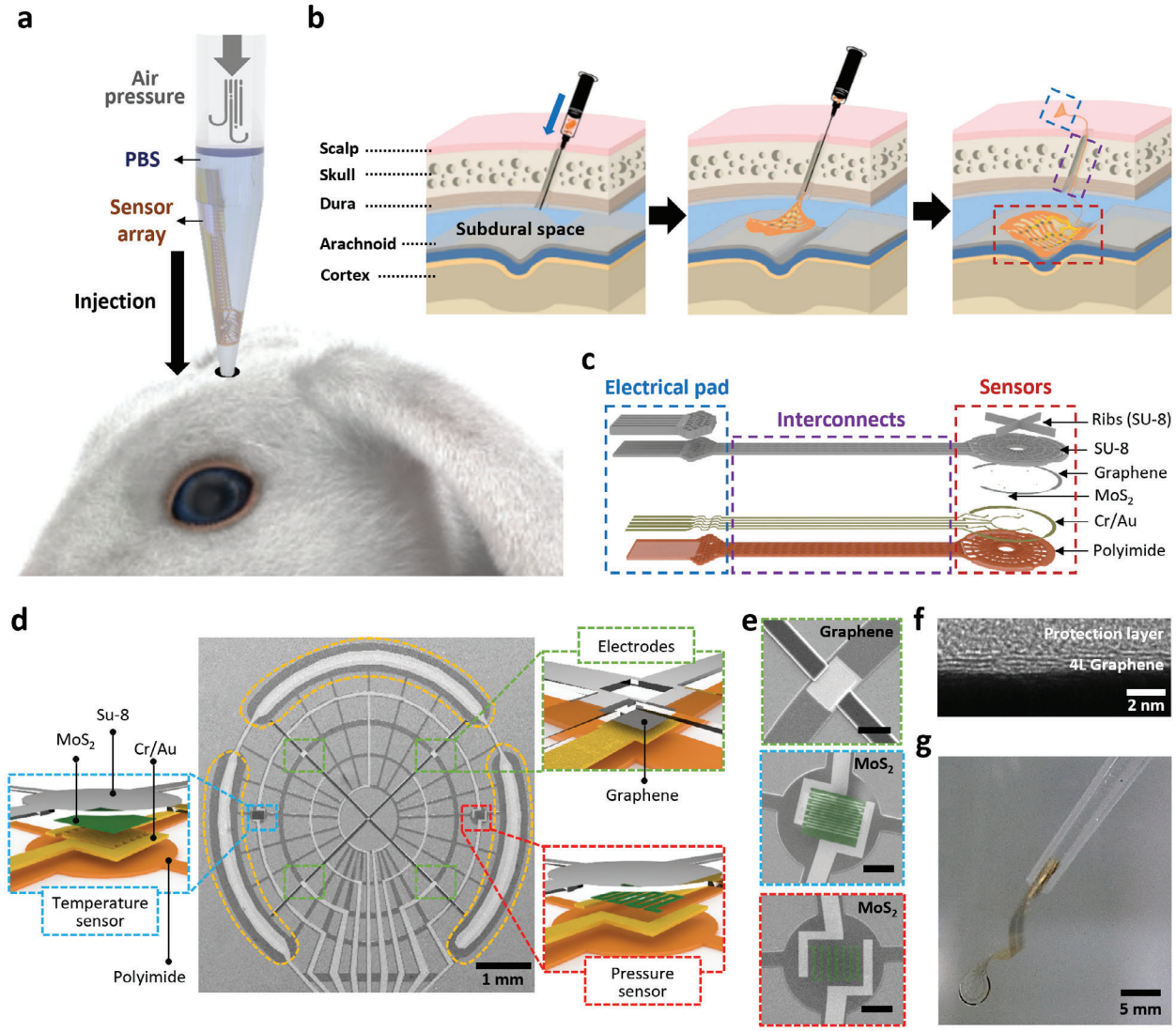

Figure 1. Schematic of sensor arrays based on 2D materials and injection process. a) Graphical illustration of conformal syringe-injectable electronics. Here, the device is loaded into a glass syringe with a buffer solution such as PBS and artificial cerebrospinal fluid. The air pressure applied by the air dispenser pushes out the buffer solution, and the flow of fluid carries the device through the syringe tip. b) Illustration of the detailed syringe injection process of electrode arrays and subsequent unfolding in the subdural space. Typically, the through-hole size is within a few millimeters in scale. The red, purple, and blue colored boxes represent the sensor, interconnects, and electrical pad, respectively. c) Layered schematic of the injectable electrode array, which is composed of SU-8 (encapsulation and ribs), graphene (electrodes), MoS_2 (multi-modal sensor), Cr/Au (interconnection) and polyimide (substrate). d) Scanning electron microscopy (SEM) image of the as-fabricated sensor part of the injectable electrode array. Additionally, detailed structures of the 4-channel graphene electrodes, MoS_2-based interdigitated temperature sensor, and serpentine pressure sensor are illustrated. e) SEM images of the electrodes and sensors for recording, stimulation, temperature, and pressure sensing. All 4-channel electrodes are composed of 4-layer graphene on gold of $70 \times 90\ \mu m^2$ in size (bright grey, top image). The middle and bottom images show the temperature and pressure sensors based on MoS_2 (green color), respectively. The size of the interdigitated temperature sensor was $175 \times 115\ \mu m^2$, with the MoS_2 film placed on interdigitated gold electrodes with a 5 μm gap and width (middle image). The MoS_2-based pressure sensor has a serpentine structure with a width of 5 μm and a length of 160 μm (bottom image). Scale bar, 70 μm. f) TEM image of the cross-section of a 4-layer graphene/gold electrode with a protection layer. g) Optical image of injectable multi-modal sensor array from a glass syringe in ×1 PBS solution.

is necessary to control the injection pressure to be within a safe range that does not damage brain cells. As it is known that pressure over 15–20 kPa can damage the brain cells (Supporting Information text 1), the pressure range must be maintained below 15 kPa.[32–35] In addition, a sufficient unfolding area fraction of at least 80% after injection is required for stable operation (Supporting Information text 1).

The bending stiffness of the mesh-structured sensor array is a key factor in engineering design. Determined primarily by the thickness of the substrate and the ribs' design, it greatly influences the mechanical dynamics of the device, such as the injection pressure, distribution of mechanical stress, and the unfolding of the substrate after ejection. For example, decreasing the thickness of the polymer substrate will reduce the bending

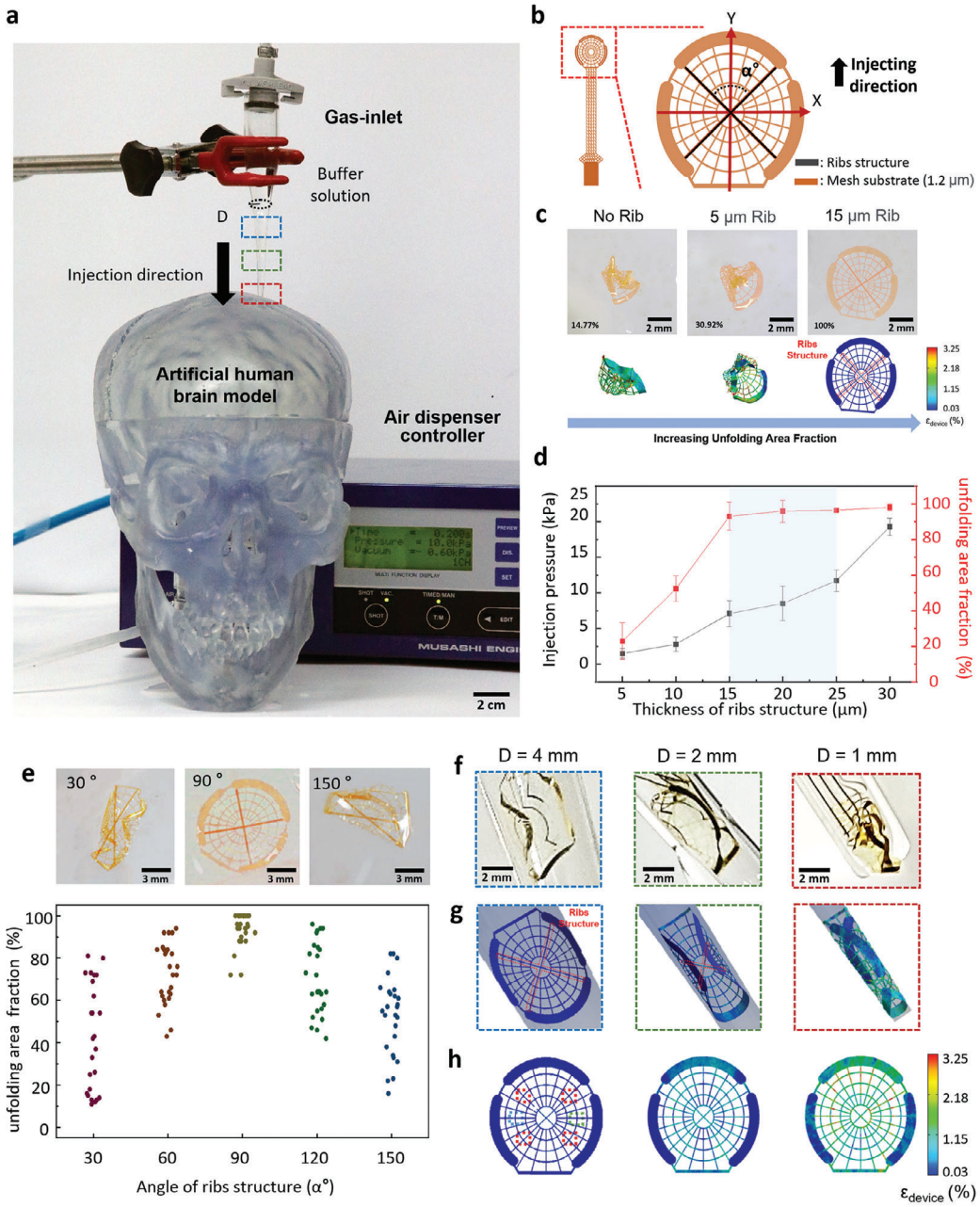

Figure 2. Validation of the ribs structure with experiments in an artificial model. a) Optical image of the injection setup with the artificial human brain model, including the air dispenser controller and the fixture for the glass syringe. Blue, green, and red dotted boxes depict the location of the device during injection where the inner diameter (D) of the syringe is 4, 2, and 1 mm. The inner diameter of the end of the syringe tip is 1 mm. Scale bar, 2 cm. b) Detailed structure of whole device and sensor with ribs and the definition of *x*- (vertical to injection direction) and *y*-axis (parallel to injection direction). The angle between two crossed lines of ribs is defined as α°. c) Optical images and corresponding simulation results of three different rib thicknesses (No rib, 5 μm rib, and 15 μm rib) after injection. The unfolding area fraction of the optical images was calculated to be 14.77%, 30.92%, and 100% (from left to right). Scale bar, 2 mm. The red dotted box represents the position of the rib structure. d) Correlation between the rib thickness, injection pressure, and unfolding yield for devices with rib structure (black/red lines, respectively). e) Three optical images at the top show the shape of the sensor part with different ribs angle α° (30°, 90°, and 150°) after injection. Scale bar, 3 mm. The bottom strip plot shows the angle dependency of the unfolding area fraction ($N = 26$ in each case). The average value of the unfolding area was calculated to be 41.3 ± 25.4%, 72.7 ± 14.3%, 93.1 ± 7.81%, 70.0 ± 16.6%, and 52.7 ± 18.3% for devices with ribs angle of 30°, 60°, 90°, 120°, and 150°, respectively. f) The optical images of the deformed state of the device during injection. The device is located where the inner diameter (D) of the syringe is measured to be 4, 2, and 1 mm, respectively. The inner diameter of the syringe tip is 1 mm. Scale bar, 2 mm. g) The simulation results of the strain distribution within the device, correlated with Figure 2f. The red dotted box represents the position of the rib structure. h) 2D mappings of the simulated strain distribution of the device during injection. This mapping was obtained from the simulation results of Figure 2g. The red, blue, and green boxes indicate the locations for the graphene electrode array, temperature sensor, and pressure sensor, respectively.

stiffness and elastic restoring force, leading to lower injection pressure and unfolding area fraction. Thus, the objective injection pressure and the unfolding area fraction must be optimized by adjusting the thickness of the substrate and rib structure. Evaluating the sole effect of mesh substrate thickness, it was observed that substrates ranging from 0.5 to 5 μm in total thickness require an injection pressure of 1–37 kPa (Figure S7a, Supporting Information). While thin substrates with a thickness of less than 3 μm could satisfy the pressure conditions for safe injection, they exhibited a low unfolding area fraction of less than 34.6% due to low elastic restoring force (Figure S7b, Supporting Information). Only thick substrates with a thickness over 5 μm could achieve a high unfolding area fraction of over 80%. However, such configurations are not feasible as the required injection pressure was well beyond the safe pressure range at 37 kPa. These results indicate that the thickness of the substrate alone cannot satisfy the requirements for both the injection pressure and the unfolding area fraction.

To solve this issue, we integrated the rib structure on the mesh substrates to enhance the elastic restoring force while minimizing the required injection pressure. The cross-shaped rib structure was designed to be much thicker than the rest of the device, which was kept thin at 1.2 μm. This design enhanced the overall bending stiffness and the elastic restoring force of the resulting structure and yet still managed to minimize the injection pressure, as most of the mesh substrate is still very thin (Figure 2b). To optimize the rib structure, the thickness and the angle ($\alpha°$) between two crossed ribs were thoroughly investigated. Without the ribs structure, the 1.2 μm thick substrate was severely crumpled upon injection and exhibited a low unfolding area fraction of 14.77% (Figure 2c top images). In contrast, devices with integrated rib structures exhibited high unfolding area fraction even at a low injection pressure of 10 kPa, owing to the improved elastic restoring force. Devices with ribs thickness of 5 and 15 μm showed a significantly improved unfolding area fraction of ≈30.92% and 100%, respectively. Mechanical simulations based on computational fluid dynamics (CFD) and finite element analysis (FEA) demonstrated a strong correlation with the experimental results, thereby proving the efficacy of the ribs structure (Figure 2c bottom images and Figure S8b, Supporting Information).[36–38] Further experiments revealed that the ribs with a thickness of 15–25 μm achieved the best result satisfying both conditions of injection pressure below 15 kPa and unfolding area fraction over 80% (Figure 2d). The angle ($\alpha°$) of the rib structure was also found to be optimal at a 90° angle. Devices with 1.2 μm-thick substrate and 15 μm-thick ribs at varying rib angles ($\alpha°$) exhibited a consistent trend where the uniaxial bending stiffness along the x-axis gradually increases with increasing rib angle ($\alpha°$), coupled with a proportional reduction along the y-axis (Figure S9, Supporting Information). Consequently, the K_x/K_y ratio, which represents the ratio of the uniaxial bending stiffness in the x and y directions, exhibited a steady increase with the increase of the rib angle. Equal bending stiffness along each axis was achieved at a 90° angle, evenly distributing the restorative force and resulting in a maximal unfolding area fraction. Similarly, the non-uniform distribution of the restorative force in the 30 and 150 devices resulted in a reduced unfolding area fraction, as shown in the optical images of Figure 2e. It is important to note that the increase in bending stiffness along the x-axis is inevitably accompanied by an increase in injection pressure, and consequently, a rise in applied strain (Figure S10, Supporting Information). Although the injection pressure of the sensor at 90° rib angle was not minimum, injection results as shown in the bottom strip plot of Figure 2e validated the significant benefits of the enhanced unfolding area fraction at 90° rib angle due to its symmetry. Each point represents the unfolding area fraction of individual devices which was obtained with the optical images of devices after each injection trial (26 trials in each group). The distribution of unfolding area fraction was most uniform at 90° rib angle, displaying the highest average value of 93.1 ± 7.81%. As the rib angle deviated from 90°, the variance increased, and the average value decreased (41.3 ± 25.4%, 72.7 ± 14.3%, 70.0 ± 16.6%, and 52.7 ± 18.3% at 30, 60, 120, and 150, respectively). As a result, a rib angle of 90° appeared to be the optimal condition, exhibiting the highest unfolding yield and ensuring a safe injection pressure.

The mesh-structured sensor array should endure severe mechanical deformation as it crumples to fit into the tip of the syringe. Figure 2f displays three optical images of the device inside a syringe with a 1 mm diameter tip, positioned at inner diameters of 4, 2, and 1 mm during the injection. The images were correlated with the mechanical simulations to estimate the applied strain on the devices during injection (Figure 2g; Figure S8a, Supporting Information). At the ejection point ($D = 1$ mm), the device displayed crumpling into a scroll-like shape to accommodate for the small diameter of the syringe tip, generating maximum strain (ϵ_{max}) on the polymeric substrate (≈3.25%). Mapping the strain distribution onto a 2D device structure, the rounded stimulation pads encircling the outer perimeter of the sensor array were found to effectively reduce the strain of substrates while maintaining structural stability (Figure 2h). Furthermore, the strain applied to the graphene and MoS_2 in the sensor array was evaluated to be 0.151% and ≈0.091%, respectively, which are lower than the known fracture tensile strain of these materials (Figure S11, Supporting Information).[20,39,40] As a result, the sensor array on the mesh substrate can exhibit stable operation without failure during the injection process (Figure S12, Video S2, Supporting Information).

2.3. Large-Scale Sensor Arrays for Enhanced Performance

Sensor arrays with a diameter of 6 mm have demonstrated a remarkable ability to be injected through a small hole in the skull, ensuring an unfolding area yield over 80% and a safe injection pressure range below 15 kPa. While this dimension is suitable for small animal experimentation, the demands for monitoring in larger animals or human subjects necessitate the exploration of sensor arrays with greater dimensions. Therefore, sensor arrays on a large scale were investigated, specifically those with diameters of 9 and 12 mm. Large sensor arrays often encounter higher strain at the narrow tip of the syringe, resulting in a lower unfolding yield and higher injection pressure. To address this issue, it was necessary to increase the thickness of the rib structure to achieve a greater elastic restoring force. **Figure 3a** shows the unfolding area fraction of devices with diameters of 6, 9, and 12 mm with ribs thickness ranging from 10 to 40 μm. The region highlighted in blue indicates that high injection

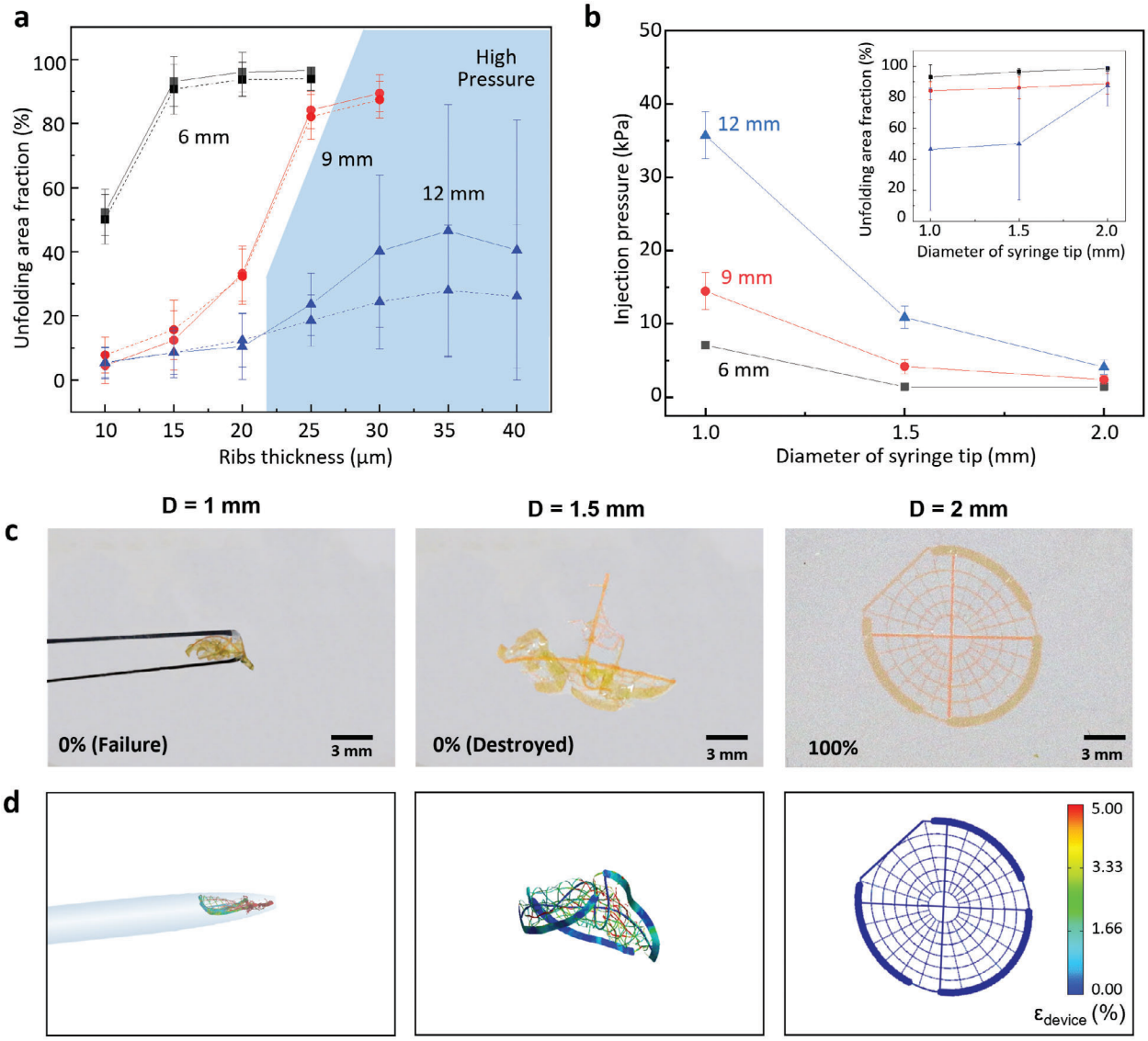

Figure 3. Injection of large-scale devices. a) Unfolding area fraction of large-scale devices with respect to varying rib thickness. The devices with diameters of 6, 9, and 12 mm were injected from syringes with a tip diameter of 1 mm. All devices were injected from two distances of 10 and 7 mm from the cortical surface in consideration of real-world conditions (solid and dashed lines, respectively). Data points in the blue region indicate that the required injection pressure for the device configuration exceeds the safe injection pressure range (>15 kPa). b) Injection pressure and unfolding area fraction (inset) of large-scale devices with respect to different diameters of the syringe tip. Black, red, and blue data correspond to 6 mm size devices with 15 μm thick ribs, 9 mm size devices with 25 μm thick ribs, and 12 mm size with 35 μm thick ribs. The thickness of the ribs was chosen based on the optimized conditions for the maximum unfolding area fraction in Figure 3A. c) Optical images of 12 mm diameter devices with 35 μm-thick ribs injected at 10 kPa from syringe tip diameters of 1, 1.5, and 2 mm, respectively. The 12 mm diameter mesh device fails to eject from the 1 mm diameter syringe tip. The device successfully ejects from the 1.5 mm diameter tip, however, shows ripped mesh components. The device injected from a 2 mm diameter tip shows successful injection and an unfolding area fraction of 100%. Scale bar, 3 mm. d) Corresponding simulation results for a 12 mm diameter mesh device injection under varying tip diameters. Similarly, the device fails to eject from a 1 mm diameter tip. 1.5 mm diameter tip shows successful ejection but fractures near impact due to high strain (>7%), which is over the fracture strain of PI. Injection from a 2 mm diameter tip shows near 100% unfolding.

pressure (>15 kPa) over the safe range was required. The devices were injected through a 1 mm diameter syringe tip at distances of 7 (dashed lines) and 10 mm (solid lines). This strategic approach is in consideration of the constraints posed by the restricted intracranial space during surgical procedures. The 6 mm devices with 15–25 μm thick ribs allowed for stable injection with a high unfolding area fraction, with an unfolding yield of up to ≈96.5%. Also, 9 mm devices with ribs thickness of 25 μm achieved over 80% unfolding area fraction at a pressure below 15 kPa (Figure S13, Supporting Information). In contrast, all 12 mm devices failed to meet the requirements with a 1 mm syringe tip, only managing to achieve a maximum of 43% unfolding area fraction with ribs thicker than 35 μm at a high pressure of 35 kPa, with many devices experiencing ejection failure or destruction.

To facilitate the safe injection of large-scale devices, the syringe tip diameter was increased to reduce the injection pressure and improve the unfolding area fraction. Using the best device parameters from Figure 3a that achieved unfolding area yield higher than 80% (6 mm diameter device with 15 μm thick ribs, 9 mm with 25 μm, 12 mm with 35 μm), injection experiments were conducted on different syringe tip diameters of 1, 1.5, and 2 mm (Figure 3b). Broadening the syringe tip diameter to either 1.5 mm or 2 mm facilitated the successful ejection of devices of all sizes. In particular, the 12 mm devices were found to be highly compatible with a 2 mm diameter syringe tip, exhibiting an unfolding area fraction of over 80% at significantly reduced pressures of 4.1 ± 1 kPa, while injection from 1 and 1.5 mm diameter tips exhibited low average unfolding area fraction of 43% and 50.1%, respectively (Figure 3b,c). 6 and 9 mm devices achieved >80% unfolding area fraction in both tip sizes, with improved unfolding at larger diameters. Mechanical simulations also confirmed the efficacy of the 2 mm diameter tip for larger devices, 12 mm in particular, with the significant reduction of crumpling in the tip area contributing to the high unfolding yield of almost 100% (Figure 3d right image, Figure S8b, Supporting Information). In contrast, when using a 1- or 1.5-mm diameter tip, significant crumpling in confined tip space led to a high strain of more than 7%, frequently resulting in ejection failures and fractures in the mesh substrate (Figure 3d left and middle images). Thus, when considering the optimization of large-scale injectable devices, careful attention should be given to both the thickness of the device and the diameter of the syringe tip.

2.4. Neural Recording and Electrotherapy in in vivo Animal Model

To evaluate the efficacy of the device under in vivo conditions, a rabbit model was utilized due to its relatively larger head size compared to rodents. Two holes of diameter ≈2 mm each for injection of the device and suction of the medium solution were drilled into the skull. The suction hole eliminated the risk of overflow from the injected solution. The suction pressure was set to a minimum to avoid affecting the device injection process (<1 kPa). Once the cerebrospinal fluid was drained, the device (6 mm diameter, 15 μm-thick ribs) was injected onto the cortical surface (**Figure** 4a; Figure S14, Supporting Information). Post-injection magnetic resonance imaging (MRI) scans vividly displayed that the injected mesh-structured sensor array had effectively unfolded and adhered to the cortical surface in the subdural space between the dura mater and the arachnoid mater (Figure 4b, Supporting Information text 2). Evaluations of the MRI image showed an unfolding area fraction of 82.7%, and further experiments verified the stable operation of the device. In addition, the injection pressure of the device was confirmed to cause no damage to the brain tissue in further injection experiments, as evidenced by the assessment of pre- and post-injection band power changes and optical inspection (Figure S15, Supporting information text 1).

The device was consequently connected to an external readout device via a flat flexible cable and a 4-channel neural recording was performed. The device successfully recorded the bicuculline-induced epileptic ECoG signals, predominantly visible in frequencies below 10 Hz. Inspection of the raw and 10 Hz filtered data clearly showed that the epileptic discharges are detected across all channels (Figure 4c,d). To emulate electrotherapy for the abnormal neural activities, standard biphasic, charge-balanced, cathodic-first electrical stimulation (200 μA amplitude, 100 μsec duration, 100 Hz frequency, 2.01 mA cm^{-2} current density) was applied via the stimulation pads, and the following neural responses were obtained (Figure 4e). Post-stimulation responses revealed noticeable reductions in the band power of delta (0.5–4 Hz) and theta bands (4–8 Hz) at −20 and −4 dB, respectively. Accompanying decreases in spike count and average amplitude were also recorded after stimulation, suggesting that the device is capable of effectively treating epileptic seizures via electrotherapy (Figure 4f). The spike count saw a reduction from 43.71 ± 4.23 to 29.86 ± 4.60 (paired sample *t*-test, $t = 7.902$, $***p < 0.001$). Moreover, the average amplitude of the spikes showed a notable decrease, plummeting from 488.69 ± 87.68 to 178.91 ± 64.63 μV ($t = 14.07$, $***p < 0.001$). Though the suppressed seizure signals still show an average of 6.2, 6.9, and 5.2 dB higher power in the delta, theta, and alpha bands in comparison with the normal state due to the lasting bicuculline dose, the seizure effects were observed to subside in >30 min, with the bandpower difference decreasing to 1, 0.9, and 1.1 dB in the delta, theta, and alpha bands. In addition, MoS_2 sensing channels were utilized to measure ICP and ICT, as it was responsive to both temperature and pressure.[41–43] A specific calibration method was implemented to calibrate the MoS_2 sensors by exploiting the difference in the temperature and pressure sensitivity according to the distinct sensor designs (text 3 and Figure S16, Supporting Information), yielding highly accurate results (Figures S17–S19, Supporting Information). The MoS_2-based ICT sensor exhibited a linear response with a relative resistance change of ≈0.014/°C and showed a highly correlated response with a commercial sensor implanted ≈2 mm adjacent to it across a range of standard intracranial temperatures in in vivo rabbit model experiments (27 to 42 °C, Figure 4g; Figure S19a, Supporting Information). The ICP sensor also exhibited a high accuracy comparable to that of commercial sensors with a linear response (6.95×10^{-6}/mmHg) in the range of 0 to 80 mmHg in in vitro experiments. Also, in the in vivo experiment, the ICP sensor successfully captured the intracranial pressure fluctuations generated by periodic abdominal compressions (Figure 4h; Figure S19b, Supporting Information).[15]

3. Conclusion

We developed a minimally invasive implantation method for the diagnosis and electro-therapy of various brain diseases using the mesh-structured sensor array with a specialized engineered structure. The mesh-structured, multi-modal sensor array with great mechanical robustness and flexibility enables efficient injection and conformal contact to the cortical surface without damage to brain tissue. Graphene multi-channel electrodes and MoS_2-based sensors on device substrates, that are conformably contacted with the cortical surface, allow for acutely detecting seizure in ECoG and electrotherapy for epileptic discharge control according to a high SNR ratio and good charge transfer efficiency and clearly monitoring ICT and ICP, respectively. This approach can reduce the surgical risk in the treatment of various

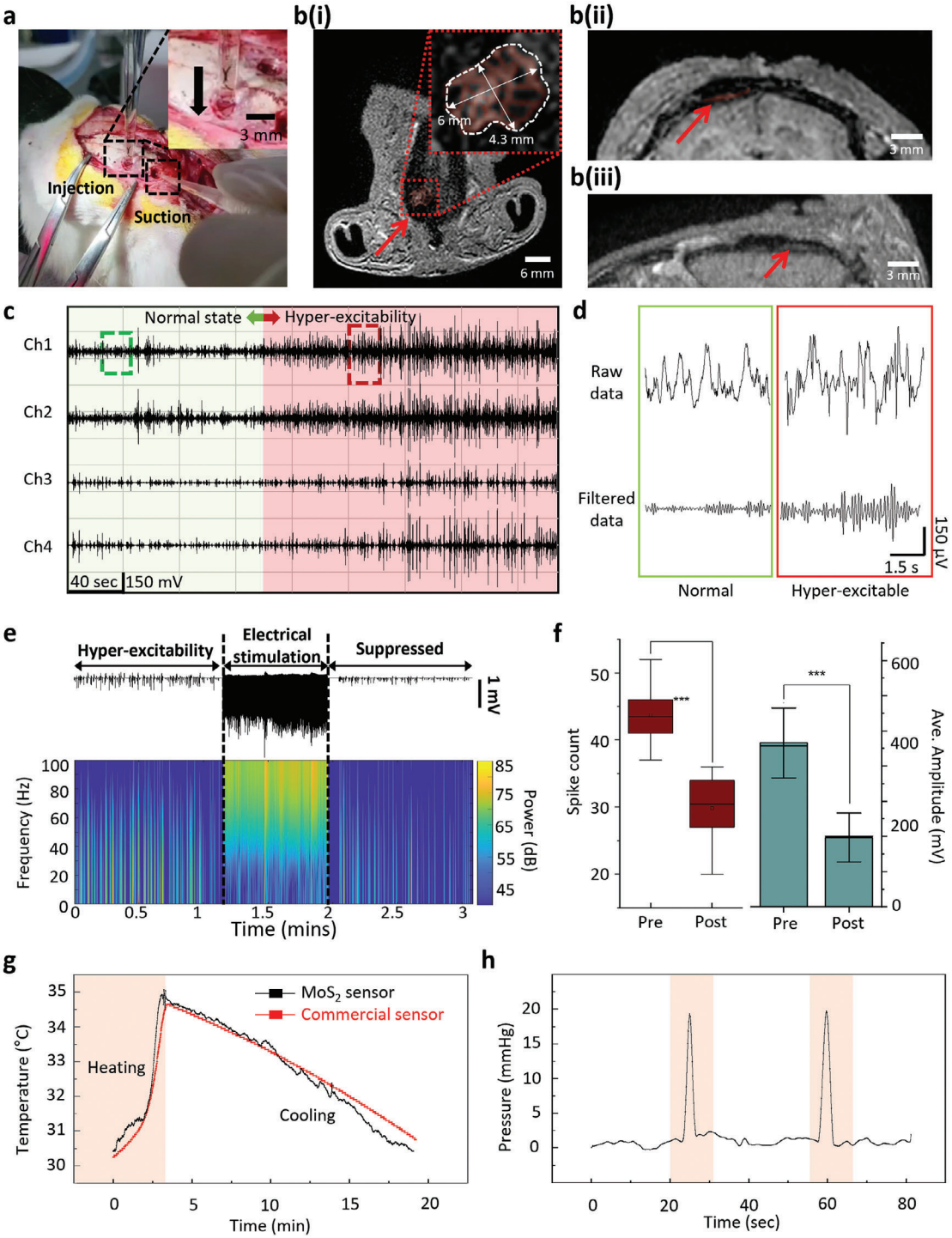

Figure 4. In vivo demonstration of injectable 2D material-based sensor array. a) In vivo demonstration of conformal syringe-injectable 2D material-based sensor array in rabbit model. Two holes were drilled for facile injection. One hole was an injection hole to inject the device, and the other hole was a suction hole to prevent the overflow of the injected solution. b) MRI results after injecting the sensor array. As shown in B(i), the sensor part of mesh electronics was well observed in the *xy* slice image. The Inset image shows a magnified image of the injected device. The image in B(ii) and B(iii) shows the side view of an injected electrode array on the brain surface shown in the *yz* and *xz* slices of the MRI. c) 4-channel neural recording data with filtered in the alpha band (8–13 Hz) before (green) and after (red) inducing the seizure by bicuculline, and d) the neural responses in the normal (green) and hyper-excitable (red) state and its filtered signal (bottom) in the alpha band. e) Raw data and short-time Fourier transformation of hyper-excitabilities, electrical stimulation, and suppressed abnormal neural signals. f) The statistical data of the treatment effect of pre/post electrical stimulation for hyper-excitable neural activity with respect to spike count and average amplitude. ***$p < 0.001$. g) in vivo measurement of ICT using the injectable device, with comparison to a commercial and rigid sensor. h) in vivo measurement of ICP using MoS_2-based sensor.

brain diseases and would lower the barrier for bio-implantable devices for the brain in the future.

4. Experimental Section

Fabrication of Free-Standing Mesh-Structured Multi-Modal Electrode Array: Single-layer graphene was grown via CVD on a Cu foil. Cu foils were heated up to 1000 °C with H_2 gas (8 sccm) at 80 mTorr for 2 h. Next, CH_4 gas (20 sccm) was injected as the precursor for 1 h and cooled at room temperature (≈25 °C) with H_2 gas (8 sccm). With a typical transfer-based multi-stacking process of graphene, four-layer (4L) graphene was formed. The monolayer MoS_2 on SiO_2/Si substrate was prepared by using low pressure chemical vapor deposition (LPCVD) methods. To form the bottom layer, the polyimide precursor was spin-coated on 80 µm thick copper substrate and baked at 250 and 300 °C for 1 and 1.5 h, respectively. Next, interconnection lines were deposited by thermal evaporation with 100 nm thick gold, which was patterned using a lift-off process. The SU-8 stiffening layer for the injection stopper was formed on the Input/Output (I/O) pad with a thickness of 5 µm. 4L graphene with a poly(methyl methacrylate) (PMMA) supporting layer was transferred to the substrate with a conventional wet transfer process. After removing the PMMA layer with acetone, the patterning process of graphene electrodes was conducted by conventional photolithography and reactive ion etching. The CVD-grown MoS_2 layer with the PMMA supporting layer was detached from the SiO_2/Si wafer on water and transferred on gold interconnections. The MoS_2 was patterned by photolithography and then etched using SF_6 plasma, which did not affect graphene. The rib mesh structure was patterned using SU-8. Finally, the SU-8 passivation layer was patterned except for the recording, stimulation electrodes, and I/O pads. After finishing the fabrication process, the handling copper substrate was dissolved with ammonium persulfate and the device was cleaned with deionized (DI) water.

Mechanical Simulations for Injection of Device: A coupled CFD-FEA approach (using Ansys Autodyn) was used to study the strain distribution on the device during injection. The setup for the injection was designed as shown in Figure S4 (Supporting Information). The pressure and initial velocity applied to the medium solution were calibrated for the ejection velocity of the sensor to match the actual experiment results. The strain distribution during the injection process was simulated and mapped onto the device structure (Figure 2g,h). To verify the stable operation of the sensors, the strain applied to different layers, the graphene and MoS_2 layers in particular, were simulated using a static FEA approach (using COMSOL Multiphysics) (Figure S7, Supporting Information). The Young's moduli (E) and Poisson ratio (ν) of the materials such as graphene, Au, Polyimide, and SU-8, which were used for the fabrication of this mesh-structured electrode array, was set as $E_{graphene} = 2.4$ TPa and $\nu_{\text{graphene}} = 0.16$, $E_{\text{MoS2}} = 242$ GPa and $\nu_{\text{MoS2}} = 0.25$, $E_{\text{Au}} = 79$ Gpa and $\nu_{\text{Au}} = 0.415$, $E_{\text{PI}} = 4$ Gpa and $\nu_{\text{PI}} = 0.34$, $E_{\text{SU-8}} = 2$ Gpa and $\nu_{\text{SU-8}} = 0.22$, respectively.

Design of the Artificial Human Brain Model: To construct an accurate human brain model, a commercial human brain model manufactured by 3B Scientific was initially acquired. However, the commercial model's composition, made of hydrophobic polymer materials, resulted in dissimilar behavior on the surface compared to that of the real brain. Consequently, the high contact angle of the phosphate-buffered saline (PBS) solution on the hydrophobic surface could potentially impact the unfolding area fraction. To overcome this limitation, it was endeavored to replicate the commercial human brain model using agarose gel, which better emulated the properties of the actual brain surface. To accomplish this, a mold was first created using the purchased brain model, based on Dragon Skin 10. This mold served as a template for the subsequent steps. A boiled agarose gel solution (0.8% concentration) was then carefully poured onto the mold and allowed to cure at a temperature range of −5–0 °C for 24 h. By doing so, an artificial brain model that closely resembled the characteristics of a real brain's surface was successfully generated. Finally, to simulate the placement of the artificial brain within a human skull, a skull model specifically designed for this purpose was utilized. The skull model featured a small hole with a diameter ranging from 1.5 to 2 mm, achieved through drilling. With the artificial brain model prepared, it was securely positioned within the skull model, enabling a comprehensive representation of the brain within its anatomical context. These measures and processes ensured that a more accurate human brain model, capable of closely mimicking the surface behavior and physical attributes of a real brain was obtained.

Set Up for Syringe Injection of Conformal Electronics: The fabricated mesh-structured electrode array was loaded into a glass syringe with phosphate-buffered saline using a stick. Then, the glass syringe was connected to a gas inlet from an air dispenser (co. Nordson EFD, Ultimus I dispenser). The connected air dispenser applied air pressure to the solution which derived the mesh-structured sensor array to be injected. The air pressure of the dispenser was regulated by two parameters: the compression pressure, responsible for ejecting the solution with the sensor array, and the suction pressure, which held the solution before injection. The exact value of air pressure was determined by subtracting the suction pressure from the compression air pressure. In this experiment, the compression air pressure was adjusted within the range of 1 to 37 kPa, while the suction pressure was maintained at ≈0.6 kPa (<1 kPa). The tip of the syringe was carefully placed on the hole of the skull and fixed using a stand. Then, the sensor array was injected by an air dispenser onto the surface of the agarose gel brain model. Considering the combined thickness of the subdural space, skull, and scalp, the total space measured ≈7 to 12 mm. The syringe tip's proximity to the scalp could also be precisely controlled within a 3 mm range to increase the available space.

In Vivo Animal Surgery: All animal handling procedures conducted in this study received prior approval from the Institutional Animal Care and Use Committee (IACUC) of Gbrain Inc. (GB-IACUC-20R08001, 21R02001, 21R06001, 22R06001) and the Institutional Animal Care and Use Committee of City University of Hong Kong (A-0117). This research complied with all the guidelines of the institution's animal welfare committee and this journal's ethics policies. Rabbits were used for in vivo experiments to guarantee enough space between the skull and cortex for the unfolding of the device. Anesthesia was carefully administered and maintained throughout the experiment using 2% isoflurane inhalation. To ensure the animals' comfort and safety, their body temperature was maintained at a stable level of 36.5 °C. Cerebrospinal fluid (CSF) was drained to ensure the space for device injection. In this procedure, a meticulous dissection of the muscles was performed, gently separating them to expose the cisterna magna located above the axis at the summit of the spinal cord. Following this, a precise incision was made in the dura, allowing for the drainage of CSF using a soft cotton material. Once the necessary CSF drainage was completed and the space was obtained, the skull was conducted to drill, resulting in a 1.5–2 mm diameter opening.

Supporting Information

Supporting Information is available from the Wiley Online Library or from the author.

Acknowledgements

J.K., J.H., and K.P. contributed equally to this work. This work was supported by the Ministry of Trade, Industry, and Energy (MOTIE) grant funded by the Korean government (MSIT) (20012355, Fully implantable closed-loop Brain to X for voice communication), the National Research Foundation of Korea (NRF-2015R1A3A2066337), and the grants from the Research Grants Council of Hong Kong (11101922) for S. Yang.

Conflict of Interest

The authors declare no conflict of interest.

Data Availability Statement

The data that support the findings of this study are available from the corresponding author upon reasonable request.

Keywords

2D materials, graphene, MoS_2, neural recording, sensors

Received: January 6, 2024
Revised: April 16, 2024
Published online: May 21, 2024

[1] J. P. Donoghue, *Nat. Neurosci.* **2002**, *5*, 1085.
[2] W. C. Stacey, B. Litt, *Nat. Rev. Neurol.* **2008**, *4*, 190.
[3] J. C. Hemphill, P. Andrews, M. D. Georgia, *Nat. Rev. Neurol.* **2011**, *7*, 451.
[4] R. S. Fisher, A. L. Velasco, *Nat. Rev. Neurol.* **2014**, *10*, 261.
[5] A. Berényi, M. Belluscio, D. Mao, G. Buzsáki, *Science* **2012**, *337*, 735.
[6] D. Khodagholy, J. N. Gelinas, T. Thesen, W. Doyle, O. Devinsky, G. G. Malliaras, G. Buzsáki, *Nat. Neurosci.* **2014**, *18*, 310.
[7] C. A. Schevon, S. K. Ng, J. Cappell, R. R. Goodman, G. McKhann, Jr, A. W., A. Branner, A. Sosunov, C. E. Schroeder, R. G. Emerson, *J. Clin. Neurophysiol.* **2008**, *25*, 321.
[8] T. Merk, V. Peterson, W. J. Lipski, B. Blankertz, R. S. Turner, N. Li, A. Horn, R. M. Richardson, W. J. Neumann, *eLife* **2022**, *11*, e75126.
[9] E. Masvidal-Codina, X. Illa, M. Dasilva, A. B. Calia, T. Dragojević, E. E. Vidal-Rosas, E. Prats-Alfonso, J. Martínez-Aguilar, J. M. De la Cruz, R. Garcia-Cortadella, P. Godignon, G. Rius, A. Camassa, E. Del Corro, J. Bousquet, C. Hébert, T. Durduran, R. Villa, M. V. Sanchez-Vives, J. A. Garrido, A. Guimerà-Brunet, *Nat. Mater.* **2019**, *18*, 280.
[10] Y. Park, C. K. Franz, H. Ryu, H. Luan, K. Y. Cotton, J. U. Kim, T. S. Chung, S. Zhao, A. Vazquez-Guardado, D. S. Yang, K. Li, R. Avila, J. K. Phillips, M. J. Quezada, H. Jang, S. S. Kwak, S. M. Won, K. Kwon, H. Jeong, A. J. Bandodkar, J. A. Rogers, *Sci. Adv.* **2021**, *7*, eabf9153.
[11] C. H. Chiang, S. M. Won, A. L. Orsborn, K. J. Yu, M. Trumpis, B. Bent, C. Wang, Y. Xue, S. Min, V. Woods, C. Yu, B. H. Kim, S. B. Kim, R. Huq, J. Li, K. J. Seo, F. Vitale, A. Richardson, H. Fang, Y. Huang, J. Viventi, *Sci. Transl. Med.* **2020**, *12*, eaay4682.
[12] J. Shin, Z. Liu, W. Bai, Y. Liu, Y. Yan, Y. Xue, I. Kandela, M. Pezhouh, M. R. MacEwan, Y. Huang, W. Z. Ray, W. Zhou, J. A. Rogers, *Sci. Adv.* **2019**, *5*, eaaw1899.
[13] M. E. Brogan, E. M. Manno, *Curr. Treat. Options Neurol.* **2015**, *17*, 327.
[14] Brain Trauma Foundation, S. L. Bratton, R. M. Chestnut, J. Ghajar, F. F. McConnell Hammond, O. A. Harris, R. Hartl, G. T. Manley, A. Nemecek, D. W. Newell, G. Rosenthal, J. Schouten, L. Shutter, S. D. Timmons, J. S. Ullman, W. Videtta, J. E. Wilberger, D. W. Wright, *J. Neurotrauma* **2007**, *24*, S37.
[15] S. K. Kang, R. K. Murphy, S. W. Hwang, S. M. Lee, D. V. Harburg, N. A. Krueger, J. Shin, P. Gamble, H. Cheng, S. Yu, Z. Liu, J. G. McCall, M. Stephen, H. Ying, J. Kim, G. Park, R. C. Webb, C. H. Lee, S. Chung, D. S. Wie, J. A. Rogers, *Nature* **2016**, *530*, 71.
[16] J. Liu, T. M. Fu, Z. Cheng, G. Hong, T. Zhou, L. Jin, M. Duvvuri, Z. Jiang, P. Kruskal, C. Xie, Z. Suo, Y. Fang, C. M. Lieber, *Nat. Nanotechnol.* **2015**, *10*, 629.
[17] A. Bonaccini Calia, E. Masvidal-Codina, T. M. Smith, N. Schäfer, D. Rathore, E. Rodríguez-Lucas, X. Illa, J. M. De la Cruz, E. Del Corro, E. Prats-Alfonso, D. Viana, J. Bousquet, C. Hébert, J. Martínez-Aguilar, J. R. Sperling, M. Drummond, A. Halder, A. Dodd, K. Barr, S. Savage, J. A. Garrido, *Nat. Nanotechnol.* **2022**, *17*, 301.
[18] J. Lee, V. Leung, A. Lee, J. Huang, P. Asbeck, P. P. Mercier, S. Shellhammer, L. Larson, F. Laiwalla, A. Nurmikko, *Nat. Electron.* **2021**, *4*, 604.
[19] D. Kuzum, H. Takano, E. Shim, J. C. Reed, H. Juul, A. G. Richardson, J. de Vries, H. Bink, M. A. Dichter, T. H. Lucas, D. A. Coulter, E. Cubukcu, B. Litt, *Nat. Commun.* **2014**, *5*, 5259.
[20] M. Park, Y. J. Park, X. Chen, Y. K. Park, M. S. Kim, J. H. Ahn, *Adv. Mater.* **2016**, *28*, 2556.
[21] G. H. Lee, Y. J. Yu, X. Cui, N. Petrone, C. H. Lee, M. S. Choi, D. Y. Lee, C. Lee, W. J. Yoo, K. Watanabe, T. Taniguchi, C. Nuckolls, P. Kim, J. Hone, *ACS Nano* **2013**, *7*, 7931.
[22] M. Lee, S. Lee, J. Kim, J. Lim, J. Lee, S. Masri, S. Bao, S. Yang, J. H. Ahn, S. Yang, *npg Asia Mater.* **2021**, *13*, 65.
[23] X. Chen, Y. J. Park, M. Kang, S. K. Kang, J. Koo, S. M. Shinde, J. Shin, S. Jeon, G. Park, Y. Yan, M. R. MacEwan, W. Z. Ray, K. M. Lee, J. A. Rogers, J. H. Ahn, *Nat. Commun.* **2018**, *9*, 1690.
[24] J. Lim, S. Lee, J. Kim, J. Hong, S. Lim, K. Kim, J. Kim, S. Yang, S. Yang, J. H. Ahn, *npg Asia Mater.* **2023**, *15*, 7.
[25] A. Bourrier, P. Shkorbatova, M. Bonizzato, E. Rey, Q. Barraud, G. Courtine, R. Othmen, V. Reita, V. Bouchiat, C. Delacour, *Adv. Healthcare Mater.* **2019**, *8*, 1801331.
[26] F. B. Haeussinger, S. Heinzel, T. Hahn, M. Schecklmann, A. C. Ehlis, A. J. Fallgatter, *PLoS One* **2011**, *6*, e26377.
[27] H. Lu, L. C. W. Lam, Y. Ning, *CNS Neurosci. Ther.* **2019**, *25*, 1270.
[28] M. S. Beauchamp, M. R. Beurlot, E. Fava, A. R. Nath, N. A. Parikh, Z. S. Saad, H. Bortfeld, J. S. Oghalai, *PLoS One* **2011**, *6*, e24981.
[29] A. Fabbro, D. Scaini, V. León, E. Vázquez, G. Cellot, G. Privitera, L. Lombardi, F. Torrisi, F. Tomarchio, F. Bonaccorso, S. Bosi, A. C. Ferrari, L. Ballerini, M. Prato, *ACS Nano* **2016**, *10*, 615.
[30] S. W. Oh, J. A. Harris, L. Ng, B. Winslow, N. Cain, S. Mihalas, Q. Wang, C. Lau, L. Kuan, A. M. Henry, M. T. Mortrud, B. Ouellette, T. N. Nguyen, S. A. Sorensen, C. R. Slaughterbeck, W. Wakeman, Y. Li, D. Feng, A. Ho, E. Nicholas, H. Zeng, *Nature* **2014**, *508*, 207.
[31] E. A. Susaki, C. Shimizu, A. Kuno, K. Tainaka, X. Li, K. Nishi, K. Morishima, H. Ono, K. L. Ode, Y. Saeki, K. Miyamichi, K. Isa, C. Yokoyama, H. Kitaura, M. Ikemura, T. Ushiku, Y. Shimizu, T. Saito, T. C. Saido, M. Fukayama, H. R. Ueda, *Nat. Commun.* **2020**, *11*, 1982.
[32] L. Siebold, A. Obenaus, R. Goyal, *Exp. Neurol.* **2018**, *310*, 48.
[33] A. M. Palmer, D. W. Marion, M. L. Botscheller, P. E. Swedlow, S. D. Styren, S. T. DeKosky, *J. Neurochem.* **1993**, *61*, 2015.
[34] H. Mao, X. Jin, L. Zhang, K. H. Yang, T. Igarashi, L. J. Noble-Haeusslein, A. I. King, *J. Neurotrauma* **2010**, *27*, 877.
[35] H. Mao, K. H. Yang, A. I. King, K. Yang, *Biomech. Model. Mechanobiol.* **2010**, *9*, 763.
[36] G. Lipkowitz, T. Samuelsen, K. Hsiao, B. Lee, M. T. Dulay, I. Coates, H. Lin, W. Pan, G. Toth, L. Tate, E. S. G. Shaqfeh, J. M. DeSimone, *Sci. Adv.* **2022**, *8*, eabq3917.
[37] H. Vahabi, W. Wang, J. M. Mabry, A. K. Kota, *Sci. Adv.* **2018**, *4*, eaau3488.
[38] M. Lin, Z. Zhang, X. Gao, Y. Bian, R. S. Wu, G. Park, Z. Lou, Z. Zhang, X. Xu, X. Chen, A. Kang, X. Yang, W. Yue, L. Yin, C. Wang, B. Qi, S. Zhou, H. Hu, H. Huang, M. Li, S. Xu, *Nat. Biotechnol.* **2023**, *42*, 448.
[39] S. H. Bae, Y. Lee, B. K. Sharma, H. J. Lee, J. H. Kim, J. H. Ahn, *Carbon* **2013**, *51*, 236.
[40] D. W. Park, A. A. Schendel, S. Mikael, S. K. Brodnick, T. J. Richner, J. P. Ness, M. R. Hayat, F. Atry, S. T. Frye, R. Pashaie, S. Thongpang, Z. Ma, J. C. Williams, *Nat. Commun.* **2014**, *5*, 5258.
[41] J. Shin, Y. Yan, W. Bai, Y. Xue, P. Gamble, L. Tian, I. Kandela, C. R. Haney, W. Spees, Y. Lee, M. Choi, J. Ko, H. Ryu, J. K. Chang, M. Pezhouh, S. K. Kang, S. M. Won, K. J. Yu, J. Zhao, Y. K. Lee, J. A. Rogers, *Nat. Biomed. Eng.* **2019**, *3*, 37.
[42] Q. Yang, S. Lee, Y. Xue, Y. Yan, T. L. Liu, S. K. Kang, Y. J. Lee, S. H. Lee, M. H. Seo, D. Lu, J. Koo, M. R. Macewan, R. T. Yin, W. Z. Ray, Y. Huang, J. A. Rogers, *Adv. Funct. Mater.* **2020**, *30*, 1910718.
[43] A. Daus, M. Jaikissoon, A. I. Khan, A. Kumar, R. W. Grady, K. C. Saraswat, E. Pop, *Nano Lett.* **2022**, *22*, 6135.